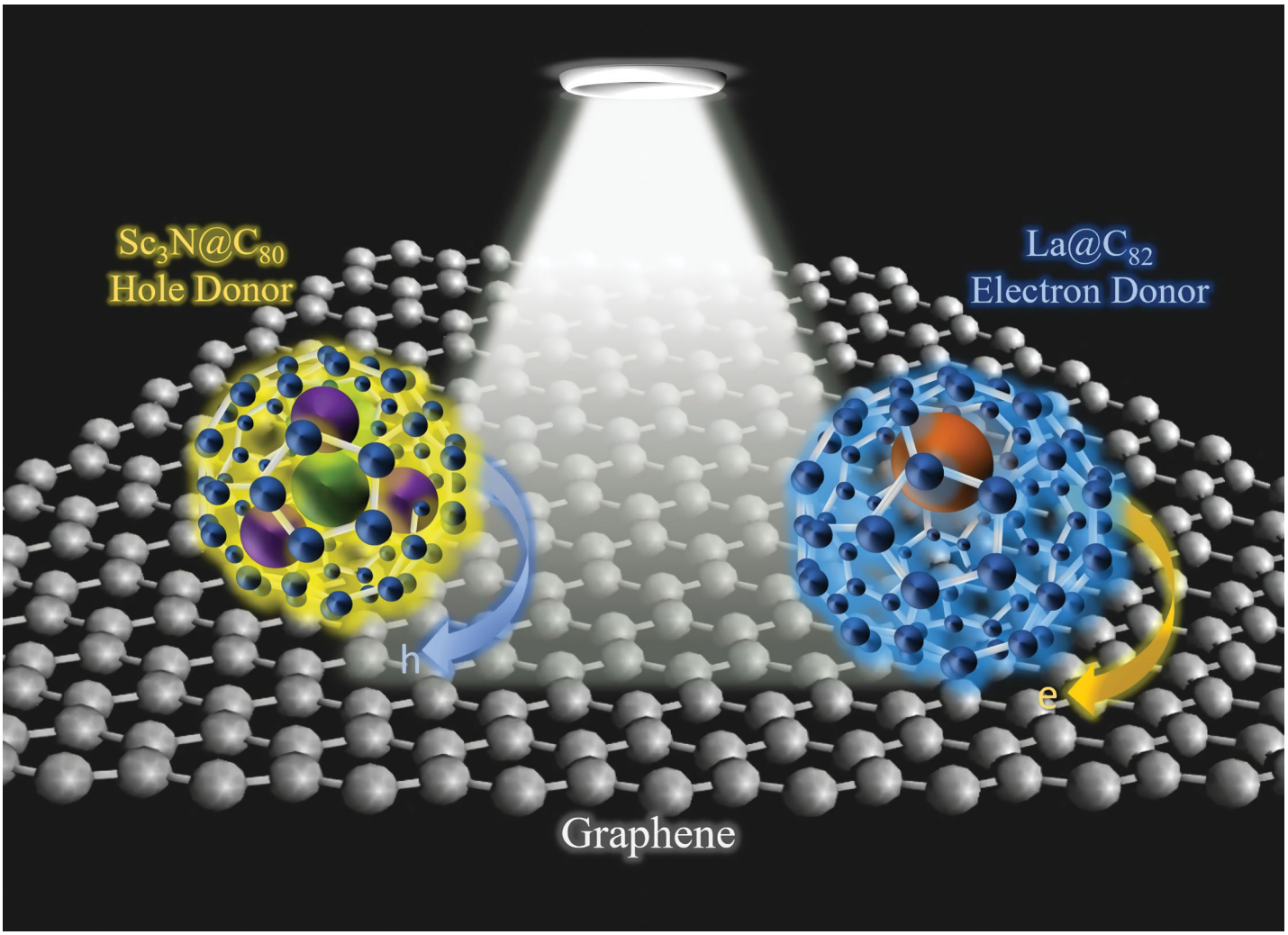

Showcasing work by the Kaul Research Group at the University of North Texas, USA

$Sc_3N@C_{80}$ and $La@C_{82}$ doped graphene for a new class of optoelectronic devices

Hybrid graphene photodetectors (PDs) with endohedral $Sc_3N@C_{80}$ and $La@C_{82}$ were used to dope graphene p-type and n-type, respectively, which resulted in significant optoelectronic property enhancement of the PDs.

As featured in:

See Luis Echegoyen, Anupama B. Kaul *et al.*, *J. Mater. Chem. C*, 2020, **8**, 3970.

ROYAL SOCIETY OF CHEMISTRY

rsc.li/materials-c

Registered charity number: 207890

Journal of Materials Chemistry C

ROYAL SOCIETY OF CHEMISTRY

COMMUNICATION

View Article Online
View Journal | View Issue

Cite this: J. Mater. Chem. C, 2020, 8, 3970

Received 9th November 2019,
Accepted 20th December 2019

DOI: 10.1039/c9tc06145b

rsc.li/materials-c

$Sc_3N@C_{80}$ and $La@C_{82}$ doped graphene for a new class of optoelectronic devices†

Kishan Jayanand,‡[a] Srishti Chugh,‡[ab] Nirmal Adhikari,[c] Misook Min,[a] Luis Echegoyen *[d] and Anupama B. Kaul *[ae]

High-performance hybrid graphene photodetectors were prepared with endohedral fullerenes deposited on graphene using electrophoretic methods for the first time. Endohedral $Sc_3N@C_{80}$, which acts as an electron acceptor, was used and the ensuing electronic and optoelectronic properties were measured. Another endohedral fullerene, $La@C_{82}$, was also adsorbed on graphene, which acts as an electron donor. Upon optical illumination, for the $Sc_3N@C_{80}$–graphene hybrid, the photoinduced free holes are injected into graphene, increasing the hole carrier concentration in graphene, while the photoexcited electrons remain in $Sc_3N@C_{80}$; this leads to a high photoresponsivity $\mathscr{R}$ of $\sim 10^9$ A W^{-1}, detectivity D of $\sim 10^{15}$ Jones, and external quantum efficiency EQE $\sim 10^9$ % for the $Sc_3N@C_{80}$–graphene hybrid. This $\mathscr{R}$ is ~10 times higher compared to other reports of quantum dot-graphene and few layer MoS_2–graphene heterostructures. Similarly, for the $La@C_{82}$–graphene hybrid, $\mathscr{R} \sim 10^8$ A W^{-1}, $D \sim 10^{14}$ Jones, and EQE $\sim 10^6$ % were achieved, with electrons being injected into graphene. The exceptional performance gains achieved with both types of hybrid structures confirms the potential of endohedrals to dope graphene for high performance optoelectronic devices using a facile and scalable fabrication process.

1. Introduction

Graphene, with its excellent electronic and optoelectronic properties, is a material of immense technological importance.[1–3] In particular, its extremely high carrier mobility of $\sim 200\,000$ cm^2 V^{-1} s^{-1} and potential for ballistic transport[4] provide opportunities for high-speed field-effect transistors (FETs),[5] compared with silicon-based FETs.[6] For its use in light detection, Sun *et al.*[4] demonstrated the first ultrafast graphene photodetector in 2010 with extremely high operational bandwidth that resulted from its outstanding electronic properties and gapless nature. However, the responsivity $\mathscr{R}$ of pristine graphene photodetectors is limited to $\sim 10^{-3}$ A W^{-1} due to its poor light absorption cross-section in active regions, short photon-generated carrier lifetimes which range in the tens of picoseconds, and the absence of a gain mechanism.[7] To overcome these challenges and enhance optical absorption, integrating semiconducting light absorbers with graphene is a viable approach for realizing high-performance graphene-based photodetectors, in which the fast exciton recombination is also minimized. Although the improvement in $\mathscr{R}$ is substantial, the performance is still not sufficient for light detection at low-intensity illumination (in the pW range), but Roy *et al.*[8] reported a MoS_2–graphene hybrid photodetector which yielded $\mathscr{R} \sim 10^8$A W^{-1} at low-intensities, down to the pW regime. After this, reports were published in rapid succession on highly sensitive photodetectors or photo-memory devices produced by hybridizing two-dimensional (2D) materials.[9]

For nanocarbon-based hybrids, photodetection using combinations of fullerenes (C_{60})–graphene,[10–17] C_{60}–nanoribbons,[13] transition-metal dichalcogenides (TMDC)–graphene,[18–20] TMDC–C_{60},[14] C_{60}–hexagonal boron nitride,[11,21,22] superatomic crystals (C_{60} and metal chalcogenides crystals),[23] fluorographene,[24] iron chloride ($FeCl_3$)–graphene[25] have been reported. C_{60} and its derivatives, *e.g.*, [6,6]-phenyl-C_{61}-butyric acid methyl ester ($PC_{61}BM$) have long been employed in solar cells because of their excellent electron-accepting abilities.[26] Endohedral fullerenes can be divided into two main groups. The first include compounds that contain atoms of non-metals or simple molecules (*e.g.*, nitrogen, phosphorus, helium, xenon, *etc.*). The second group includes endohedral fullerenes which encapsulate metal ions or metal-containing clusters.[27,28] The discovery of

[a] Department of Materials Science and Engineering, PACCAR Technology Institute, University of North Texas, Denton, TX 76203, USA. E-mail: anupama.kaul@unt.edu
[b] Department of Metallurgical, Materials and Biomedical Engineering, University of Texas at El Paso, El Paso, TX 79968, USA
[c] Department of Electrical Engineering, University of Texas at El Paso, El Paso, TX 79968, USA
[d] Department of Chemistry, University of Texas at El Paso, El Paso, TX 79968, USA. E-mail: echegoyen@utep.edu
[e] Department of Electrical Engineering, University of North Texas, Denton, TX 76203, USA

† Electronic supplementary information (ESI) available. See DOI: 10.1039/c9tc06145b
‡ These authors contributed equally to the work.

endohedral cluster fullerenes in 1999 signalled a significant turning point in fullerene research, favoured by the high synthetic yields achieved and the interest in their fundamental chemical and electronic properties.[27]

For exploring the interactions with graphene, we selected a cluster endohedral fullerene, $Sc_3N@C_{80}$, denoted as END_1 here, and monometallic endohedral fullerene, $La@C_{82}$, denoted as END_2 here, based on their electron-accepting and electron-donating abilities, respectively.[28] The END_1 is very stable under ambient conditions and can be produced in high yields.[29–31] Similar to C_{60}, END_1 has also been used as an electron-acceptor in organic photovoltaic (OPV) cells to enhance power conversion efficiencies.[32–34] Recently, Xu *et al.*[35] reported the first successful and facile preparation of micron-sized hexagonal single crystalline END_1 rods using the liquid–liquid interfacial precipitation (LLIP) method for photo-electrochemical applications, which clearly demonstrates its efficient charge carrier transport properties and confirms its potential for photo-electric conversion.

The END_2 in this work is also produced by the carbon arc method but the yield is far lower.[36] END_2 features a large anionic π surface and an open-shell structure. Importantly, in comparison to the C_{60} absorption spectrum with peaks between the ~400–700 nm range[37] and the END_1 absorption spectrum between ~450–680 nm,[38] the broad absorption of END_2 from ~600–1100 nm clearly highlights its enhanced optical absorption well into the infra-red regime.[39] While bonding and dynamics of metal atoms inside the endohedral cages have been examined in the past, END_2 has received comparatively little attention owing largely to its lower production yields.[40,41]

Despite the potential advantage of endohedrals in OPV, their integration in graphene-based devices remains essentially unexplored. Herein, for the first time, we report the combination of zero-dimensional (0D) END_1 and END_2 with 2D graphene to yield hybrid systems, where charge transfer processes result in the emergence of interesting optoelectronic properties. The Raman shift in the G- and 2D-modes of the hybrids relative to bare graphene, confirms that hole-doping is occurring in graphene with END_1, while electron-doping occurs with END_2. From our analysis we conclude that charge transfer and consequent photocurrent I_{ph} generation contribute to a high $\mathscr{R}$ of $\sim 10^9$ A W^{-1} and $\sim 10^8$ A W^{-1} in the END_1–graphene and END_2–graphene, respectively, over wavelengths λ of 400 to 1100 nm. The $\mathscr{R}$ for END_1–graphene reported in this work is ~10 times higher compared to the MoS_2–graphene heterostructure photodetectors with $\mathscr{R} \sim 10^8$ A W^{-1} reported previously.[8]

2. Results and discussion

2.1 Graphene–$Sc_3N@C_{80}$ hybrid

The electrophoretic deposition technique was used to deposit ~1 mg mL^{-1} END_1 in *ortho*-dichlorobenzene (*o*-DCB) on top of the graphene membrane and the device was vacuum annealed for ~24 hours at ~180 °C (Fig. S1, ESI†). Insights into the structural morphology of END_1 agglomerated on top of the graphene membrane was obtained using Scanning Electron Microscopy (SEM) and Atomic Force Microscopy (AFM) (Fig. S2, ESI†). The influence of annealing on the optical characteristics of the device has not been evaluated presently, but will be interesting to pursue for a future study. The bare graphene thickness was ~24 nm measured using AFM indicating the presence of multi-layer graphene (MLG), as shown by the height profile scan in the inset of Fig. S2(e)–(i) (ESI†). Fig. S2(f)(i) and (ii) (ESI†) illustrate the clusters of bare END_1 in the form of islands exhibiting a peak height of ~3.6 nm and diameter ~50 nm. On the other hand, Fig. S2(g)(i)–(ii) (ESI†) reveals clustering of END_1 on the graphene surface with a peak height of ~9–20 nm and cluster diameter ~200–350 nm.

The bare END_1, bare graphene, and END_1–graphene hybrid assemblies were further characterized using Raman spectroscopy, as well as temperature T dependent Raman, which is a non-invasive characterization technique used for inferring the structural and electronic properties of materials.[42] Fig. 1(a) shows the Raman spectra of END_1–graphene hybrid at room T which is compared to bare graphene, while the inset shows the Raman spectra of the bare END_1 with a central peak at 1203 cm^{-1} and a relative normalized peak intensity $I_{END_1} \sim 1$ a.u. This peak is blue-shifted $\Delta\omega^{(+)}$ by ~50 cm^{-1} for the END_1–graphene Raman hybrid (with relative normalized peak intensity for $I_{END_1} \sim 0.4$ a.u., as shown) and is attributed to the van der Waals interaction between END_1 and the graphene membrane.[30] Fig. 1(b) and (c) show the magnified G- and 2D-bands of END_1–graphene relative to bare graphene, respectively, at room T. The $\Delta\omega^{(+)}$ shift for the G-band and 2D-band were measured to be ~5 cm^{-1} and ~10 cm^{-1}, respectively. The $\Delta\omega^{(+)}$ shift for the G- and the 2D-band for END_1–graphene observed here is similar to the $\Delta\omega^{(+)}$ shift for the G- and the 2D-band for C_{60}–graphene hybrids reported by Jnawali *et al.*[10] The $\Delta\omega^{(+)}$ shift is attributed to C_{60} causing p-type doping in graphene that has been confirmed using THz-time domain spectroscopy.[10] Thus, from the $\Delta\omega^{(+)}$ shift for the G-band and 2D-band of END_1–graphene, it can be inferred that END_1 also induces p-doping in graphene. This assertion is in alignment with the oxidation potential of END_1 which is ~0.59 mV, measured using cyclic voltammetry, implying that END_1 is a p-type dopant.[39] Besides using Raman Spectroscopy to deduce doping effects, three terminal devices with back gating can also allow for the verification of doping on a future study.

The T-dependent Raman spectra of graphene and of the END_1–graphene hybrid were measured from $T \sim 298$ K to ~873 K and the data are plotted in Fig. 1(d). The G-band peak position experienced a red shift with temperature, where a $\Delta\omega[T]^{(-)}$ shift of ~14 cm^{-1} (~1580 cm^{-1} at $T \sim 298$ K to ~1566 cm^{-1} at $T \sim 873$ K) for bare graphene (bottom plot of Fig. 1(d)) was observed as T increased from ~298 K to ~873 K. A similar $\Delta\omega[T]^{(-)}$ shift of ~23 cm^{-1} (~1586 cm^{-1} at $T \sim 298$ K to ~1563 cm^{-1} at $T \sim 873$ K) was also observed for the END_1–graphene hybrid (top plot of Fig. 1(d)) as T increases. The G-band shift towards lower frequencies is attributed to optical phonon softening as T increases given that the G-band is intimately associated with optical phonons which are very

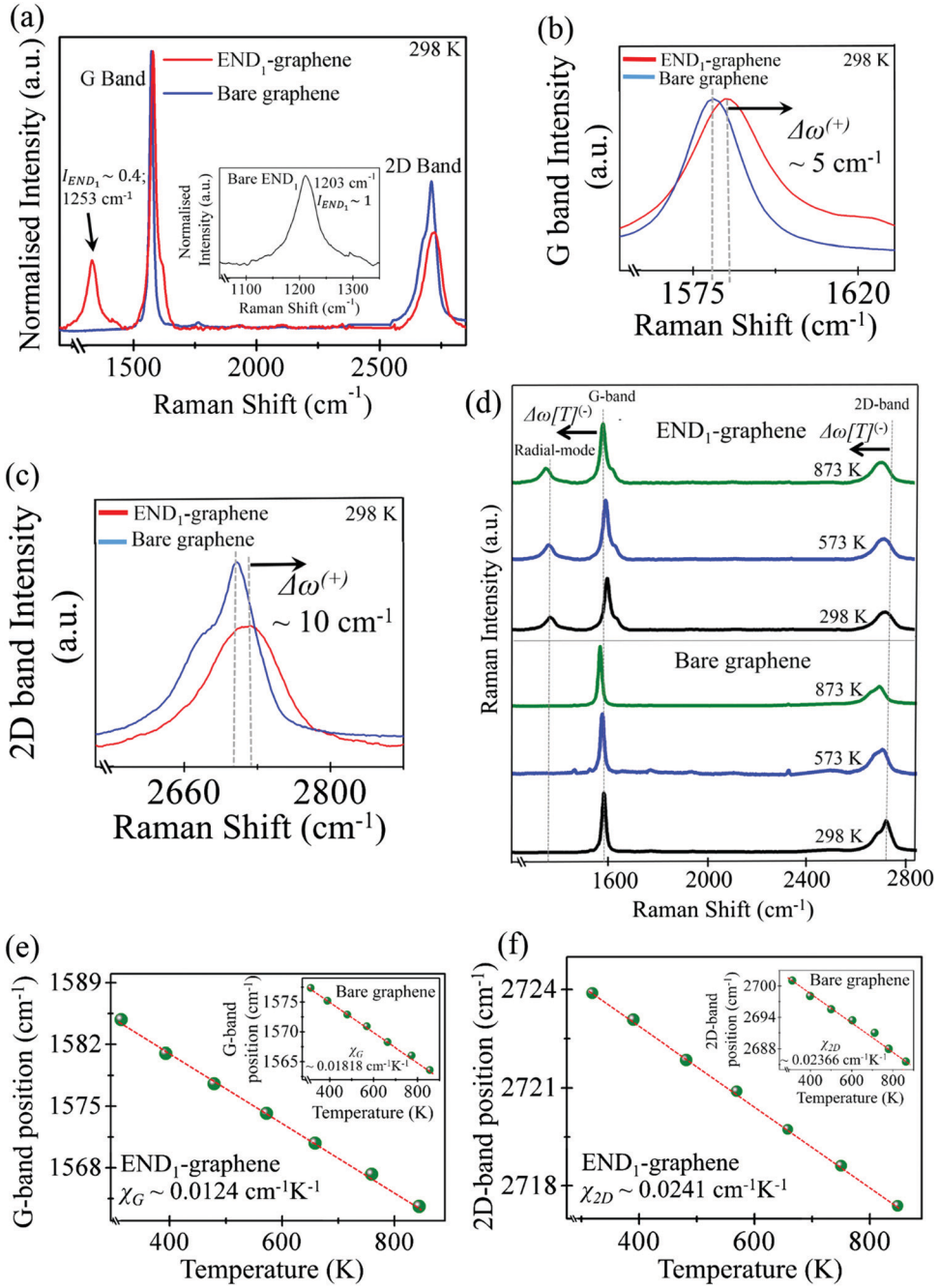

Fig. 1 (a) Raman spectra of END_1–graphene hybrid and bare graphene at room T. Inset shows the Raman spectra of the bare END_1 film. The peak at ~1203 cm^{-1} in the inset is the tangential mode of END_1 with a relative normalized peak intensity $I_{END_1} \sim 1$ a.u. This peak is blue-shifted $\Delta\omega^{(+)}$ by ~50 cm^{-1} in the END_1–graphene Raman spectra, as shown (with relative normalized peak intensity for $I_{END_1} \sim 0.4$ a.u.) and is attributed to the van der Waals interaction between the END_1 and the graphene membrane. The mechanically exfoliated graphene membranes show an intense tangential mode G-band at ~1580 cm^{-1} and a 2D-band at ~2714 cm^{-1}. (b) and (c) are the magnified G- and 2D-band peaks, respectively, for graphene and END_1–graphene. The G-peak of graphene experiences a $\Delta\omega^{(+)}$ shift of ~5 cm^{-1} and for the 2D-peak the $\Delta\omega^{(+)}$ shift is ~10 cm^{-1} which is due to the p-type doping induced in graphene by END_1. (d) Variation of the G- and 2D-band with T in the END_1–graphene hybrid (top) and bare graphene (bottom). Its clear that a red-shift $\Delta\omega[T]^{(-)}$ is seen in both cases for the G- and 2D-bands as T increases. (e) Linear fit (dotted red lines) showing the extracted χ_G for the G-band, and (f) χ_{2D} for the 2D-band in END_1–graphene. Insets in (e) and (f) show the respective values for bare graphene. In this case $\chi_G < \chi_{2D}$ (~0.01818 cm^{-1} K^{-1} $\lesssim$ 0.02366 cm^{-1} K^{-1} for bare graphene and ~0.0124 cm^{-1} K^{-1} $\lesssim$ 0.0241 cm^{-1} K^{-1} for END_1–graphene).

sensitive to carrier density.[43] Similarly, the 2D-band peak experiences a $\Delta\omega[T]^{(-)}$ shift of ~14 cm^{-1} for bare graphene (~2701 cm^{-1} at $T \sim 298$ K to ~2683 cm^{-1} at $T \sim 873$ K) (bottom of Fig. 1(d)), and the END_1–graphene hybrid also underwent a $\Delta\omega[T]^{(-)}$ shift of ~16 cm^{-1} (~2714 cm^{-1} at $T \sim 298$ K to ~2698 cm^{-1} at $T \sim 873$ K) (top plot of Fig. 1(d)). Incidentally, the 2D-band is sensitive to changes in the electronic band structure such as that arising from strain,

which in this case would imply temperature-induced strain changes for the bare graphene and for the END_1–graphene hybrid.[44]

The Raman shifts of the G-band and 2D-band as a function T were further analysed by extracting the fitting parameters when the data are fit to $\omega = \omega_0 + \chi T$; here ω_0 is the extrapolated peak position at 0 K, and χ is the first-order T-coefficient. From the linear fit for the G-band and the 2D-band for END_1–graphene shown in Fig. 1(e) and (f), respectively, the first-order T coefficients for bare graphene were calculated to be $\chi_G \sim 0.01818\ cm^{-1}\ K^{-1}$ and $\chi_{2D} \sim 0.02366\ cm^{-1}\ K^{-1}$ (insets in Fig. 1(e) and (f)). Equivalently, the T-coefficients for the END_1–graphene hybrid were $\chi_G \sim 0.0124\ cm^{-1}\ K^{-1}$ and $\chi_{2D} \sim 0.0241\ cm^{-1}\ K^{-1}$. In our case $\chi_G < \chi_{2D}$ ($\sim 0.01818\ cm^{-1}\ K^{-1} \lesssim 0.02366\ cm^{-1}\ K^{-1}$ for graphene, and $\sim 0.0124\ cm^{-1}\ K^{-1} \lesssim 0.0241\ cm^{-1}\ K^{-1}$ for END_1–graphene) which is consistent with a previous report by Tian *et al.*[43] who determined $\chi_G \sim 0.01496\ cm^{-1}\ K^{-1} < \chi_{2D} \sim 0.02484\ cm^{-1}\ K^{-1}$ for graphene, and explained this result on the basis of the "self-energy" contribution from the G-band.

The I–V measurements of the END_1–graphene hybrid were conducted in a vacuum probe stage at a pressure of $\sim 10^{-6}$ Torr, where T was controlled from ~ 5.8 K to 298 K using a closed-cycle He refrigerator and the results were compared to those of bare END_1 and bare graphene, as shown in Fig. 2(a). At $T \sim 298$ K, the transport current I is ~ 20 times higher for END_1–graphene relative to bare graphene and bare END_1, as the data in Fig. 2(a) reveal. In Fig. 2(b), the I increased from ~ 12 mA at $T \sim 5.8$ K to ~ 24 mA at $T \sim 298$ K for $V \sim 1$ V for the END_1–graphene hybrid, while in Fig. 2(c), the I increases from ~ 0.38 mA at $T \sim 5.8$ K to ~ 0.8 mA at $T \sim 298$ K for bare graphene at $V \sim 1$ V. Similarly, in the inset of Fig. 2(c) for bare END_1, I increases from ~ 0.5 mA at $T \sim 5.8$ K to ~ 2.1 mA at $T \sim 298$ K. These data clearly show that the device resistance R for the bare END_1, bare graphene, and END_1–graphene hybrid decreases as T increases and that the adsorption of END_1 results in modulation of the electronic transport in graphene. The dependence of R with T is further delineated by the data in Fig. 2(d), where the inset shows the R–T Characteristic of bare graphene, bare END_1 and the END_1–graphene hybrid. An inverse correlation of R with T is evident for all three cases, as shown in the inset of Fig. 2(d) with some nonlinearities present. Defects in bare graphene may be responsible for the inverse T-dependence of R which has been previously reported,[45] and in the case of END_1–graphene may also arise from the p-type doping induced.[46] Additionally, for bare END_1 as T increases, the charge carriers in END_1 have a higher likelihood of overcoming the potential barrier and thus decreasing R.[33] Liu *et al.*[47] used the Efros–Shklovskii model to calculate the activation energy E_a of

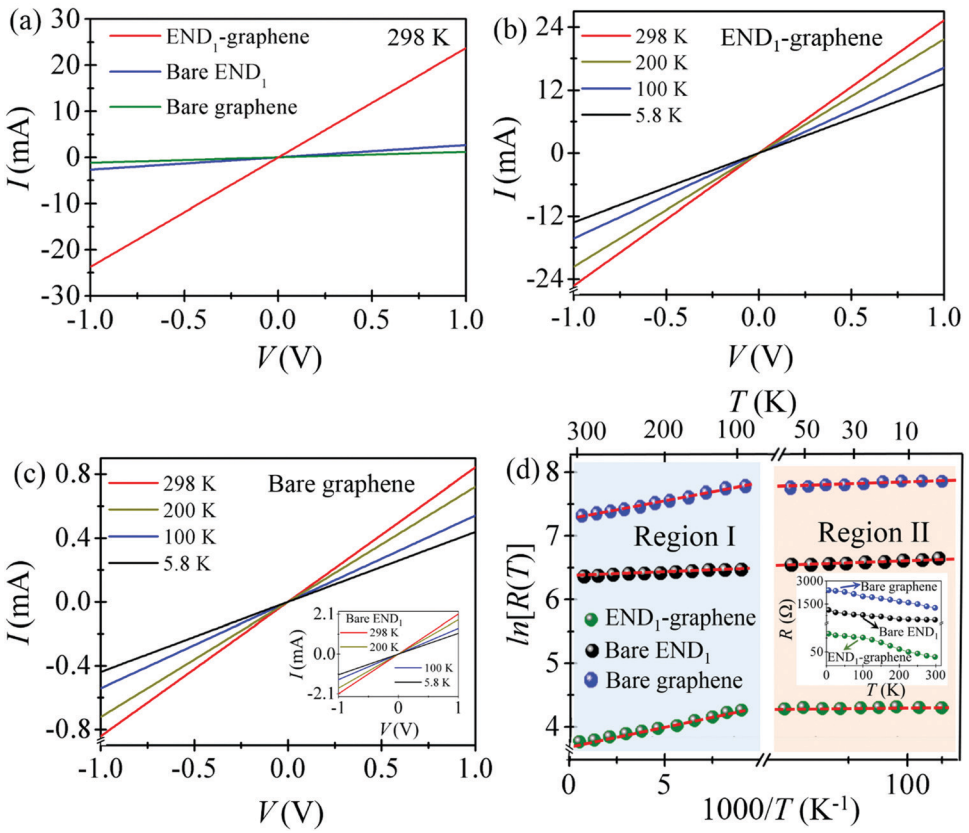

Fig. 2 The I–V of (a) END_1–graphene, bare END_1, and bare graphene at $T \sim 298$ K. The I–V of (b) END_1–graphene, (c) bare graphene, and END_1 (inset) over various temperatures. (d) Logarithmic plot of ln[$R(T)$] as a function of 1000/T. Two regions were used to plot $ln[R(T)]$ as a function of 1000/T, namely Region I (65–298 K) and Region II (5.8–60 K), showing the linear fit of the data (solid red lines). The inset shows a non-linear R *versus* T plot for bare graphene, bare END_1, and END_1–graphene. The E_a values were extracted from this fit and the results are summarized in Table 2.

few-layer graphene interconnects, but the fit encompassed significant uncertainty for T from ~5–340 K. Therefore, in our analysis we consider two distinct regions shown in Fig. 2(d) from T ~ 65–298 K (Region I), and from T ~ 5.8–60 K (Region II), where the data are fit to the Arrhenius model[48] denoted by eqn (1) below,

$$R(T) = R_0 \exp\left[\frac{E_a}{2kT}\right] \quad (1)$$

Here $R(T)$ is the resistance at T, R_0 is the resistance at $T = \infty$ and is referred to as the pre-exponent, E_a is the thermal activation energy, and k is the Boltzmann constant. Eqn (1) is rewritten as,

$$\ln R = \ln R_0 + \frac{E_a}{2kT} \quad (2)$$

where a linear relationship is expected between the $\ln[R(T)]$ *versus* T plot. As noted, two regions were used to plot $\ln[R(T)]$ as a function of $1000/T$, shown in Fig. 2(d) where E_a is deduced from the slope of this fit. Table 1 summarizes the E_a values tabulated for Region I (~65–298 K) and Region II (~5.8–60 K), along with the r^2 values where r is the correlation coefficient, for bare graphene, bare END_1, and the END_1–graphene hybrid. For Region I, E_a was tabulated to be ~0.73 meV for bare graphene, ~0.54 meV for bare END_1, and ~0.43 meV for END_1–graphene. Similarly, for Region II, E_a ~ 0.94 meV for bare graphene, ~0.76 meV for bare END_1, and ~0.61 meV for END_1–graphene were determined. We believe the physical origin of the different activation energies comes from two mechanisms that maybe operative. The first is likely due to a thermally activated hopping mechanism related to defects in the underlying graphene, which is dominant at the lower temperatures (Region II) with the larger activation energies. The defects in the underlying graphene in our END_1–Graphene hybrid are likely to contribute to Region II's larger activation energy, and hence larger resistance, where dopants maybe largely frozen out. In the higher temperature regime (Region I), the dopants have a higher likelihood for getting activated due to increased thermal energies which would result in an increase in charge carrier density, conductivity, reduced resistance and hence lower activation energy, as noted in Table 1 by the activation energy values we have tabulated. The E_a values for the hybrid structures are lower by ~41% and ~35% for both Region I and Region II, respectively, when compared to bare graphene. This reduction in E_a is consistent with the p-type doping induced in graphene as a result of interactions with END_1, and is also inferred from the $\Delta\omega[T]^{(-)}$ shift of the Raman spectrum (Fig. 1(a)).

Table 1 The activation energy E_a and correlation coefficient r^2 fitting values for bare graphene, bare END_1, and END_1–graphene hybrid for Region I (~65–298 K) and Region II (~5.8–60 K). The E_a was lowest for the END_1–graphene hybrid

	Region I (65–298 K)		Region II (5.8–60 K)	
Device	E_a (meV)	r^2	E_a (meV)	r^2
Bare graphene	~0.73	~0.915	~0.94	~0.994
Bare END_1	~0.54	~0.918	~0.76	~0.992
END_1–graphene	~0.43	~0.925	~0.61	~0.993

The END_1–graphene and bare END_1 devices were exposed to a white light source to initiate the optoelectronic transport measurements of these devices under vacuum. The I_{ph} was extracted from the measurements done in the dark (*i.e.* I_{dark}) and in the presence of light (*i.e.* I_{light}) where $I_{ph} = I_{light} - I_{dark}$. Under illumination, as shown in Fig. 3(a), the I_{light} values were ~10 times higher for the hybrid (~25.15 mA at 0.5 V) compared to the bare END_1 (inset) where I_{light} ~ 2.5 mA at 0.5 V at room T. We note here that our devices are based on a two-terminal device architecture where the photoconductive mechanism (no gate voltage applied) is operative, unlike in prior work[8,12,24,49–51] that relied on an external gate voltage applied, based on a three-terminal device architecture. Fig. 3(b) shows the time-dependent I_{ph} measurements of bare END_1, bare graphene, and the END_1–graphene hybrid at ~1 V (where I_{light} ~ 26.43 mA and I_{dark} ~ 25.20 mA for END_1–graphene, and I_{light} ~ 2.82 mA and I_{dark} ~ 2.07 mA for END_1). The cycles in yellow refer to the ON-state of the light pulses, while the OFF-cycles (no color) represent the absence of light. A photoresponse was not detectable in our bare graphene device, as the I_{ph} was below the pico-amp range (secondary y-axis). As reported earlier, in graphene, a short photon-generated carrier lifetime persists on the scale of picoseconds, and the ON/OFF ratio is also quite poor.[8] Fig. 3(c) shows the response of the photocurrent over a single ON-pulse, where the rise time τ_r and decay time τ_d for bare END_1 and END_1–graphene are measured. The τ_r and τ_d are among the figures of merit that are important to gauge the photodetector response. The τ_r is measured from ~10% of the noise floor and ~90% of the peak signal value. Similarly, τ_d was computed from ~90% to 10% of the maximum and minimum signal intensities, respectively.[52] These values were τ_r ~ 1.8 ms and τ_d ~ 2.7 ms for the END_1–graphene hybrid, and for bare END_1, τ_r ~ 2.6 ms and τ_d ~ 3.1 ms. The response time for our END_1–graphene hybrid is significantly lower compared to PbS QDs–graphene hybrids (τ_r ~ 10 ms and τ_d ~ 20 ms)[49] and Bi_2Te_3–graphene hybrids (τ_r ~ 8.7 ms)[51] as photodetectors reported previously.

The $\mathscr{R}$ for END_1–graphene and bare END_1 was calculated using $\mathscr{R} = \frac{I_{ph}}{P}$, where P is the incoming power, and the values were determined to be ~4×10^9 A W^{-1} and 2×10^8 A W^{-1} at ~1 V and P ~ 3.3 pW at room T, respectively, with an incoming light power density (calibrated using the Thorlabs optical power meter PM100D) ~3 mW cm^{-2}. Fig. 3(d) shows the band diagram illustrating the charge transport between the END_1–graphene interface at equilibrium (top of Fig. 3(d)) and upon illumination (bottom of Fig. 3(d)). The lowest unoccupied molecular orbital energy (LUMO) of END_1 is ~−4.6 eV, while the HOMO level is ~−5.7 eV.[53] Upon illumination, the incident photons excite ground-state electrons of END_1 into excited states. Electron–hole pairs are then formed at the END_1–graphene interface and photogenerated holes are efficiently injected into the graphene; thus, END_1 is a p-type dopant with graphene which is also consistent with the high oxidation potential of END_1 ~ 0.59 mV.[39] This leads to an increase in the hole carrier density as the hole population in graphene

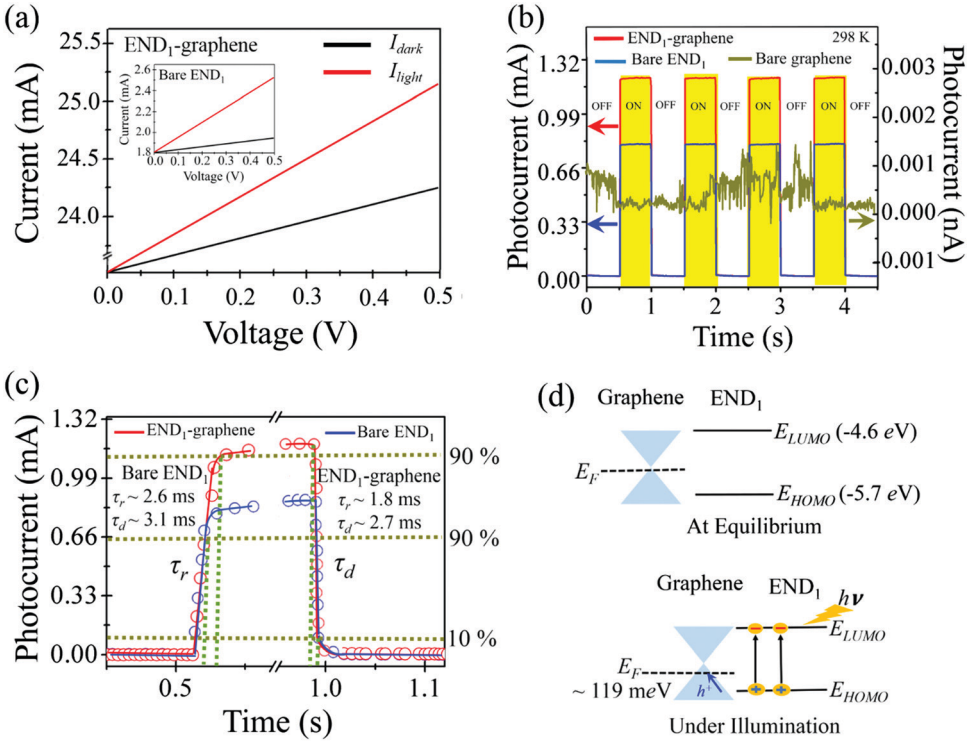

Fig. 3 (a) The I–V response of END$_1$–graphene and bare END$_1$ (inset) in the dark and illuminated states where a white light source was used for illumination in vacuum at room T. (b) The I_{ph} was extracted from the measurements done in the absence and presence of light over multiple ON (yellow) and OFF (no color) cycles (where, $I_{light} \sim 26.43$ mA and $I_{dark} \sim 25.20$ mA for END$_1$–graphene, and $I_{light} \sim 2.82$ mA and $I_{dark} \sim 2.07$ mA for END$_1$) at ~ 1 V. The bare graphene device yields a nondiscernable photoresponse, as shown by the secondary y-axis. (c) A magnified single ON-cycle pulse, where the τ_r and τ_d were calculated. Left and right insets list the values of τ_r and τ_d for bare END$_1$ and END$_1$–graphene, respectively. (d) Schematic representation of the band diagram for graphene and END$_1$ at equilibrium (top) and under illumination (bottom) illustrating the hole transfer from END$_1$ to graphene. The E_F of graphene experiences a downward shift by ~119 meV.

increases,[10] as shown schematically in Fig. 3(d). The injection of holes leads to the downward shift in E_F in graphene,[54] and to electron injection into END$_1$, where charge neutrality is maintained in the hybrid. Flores *et al.* reported that hole-doping in exfoliated graphene using various process treatments shifts E_F, and E_F and carrier concentration (N) at room T are determined from the shift in the Raman peak positions using eqn (3) and (4) below,[55]

$$E_F\ (\text{eV}) = \left|\frac{\text{Position(G-band)} - 1580}{42}\right| \quad (3)$$

$$N\ (\text{cm}^{-2}) = \frac{\left(\frac{E_F}{\hbar \nu_F}\right)^2}{\pi} \quad (4)$$

Position (G-band) refers to the peak position of the G-band which occurs at 1585 cm^{-1} for the hybrid (from Fig. 1(b)), $\nu_F = 1.09 \times 10^6$ m s^{-1} is the Fermi velocity and $\hbar$ is the modified Planck's constant (*i.e.* $\hbar = h/2\pi$, where $h = 6.626 \times 10^{-34}$ J s). From our Raman data in Fig. 1(b), we calculated a value for $E_F \sim 119$ meV and accordingly $N \sim 8.5 \times 10^{11}$ cm^{-2} at ~298 K. The results are also consistent with the observed $\Delta\omega^{(+)}$ shift for the G-band in Fig. 1(b), which is attributed to hole-doping in graphene, and in turn induces the downward shift in E_F in graphene.[56]

To further explore the photodetector response, a tunable laser source, the Fianium LLFT Contrast (NKT Photonics), was used for optical excitation, and wavelength λ was increased in ~100 nm increments from 400–1100 nm. Fig. 4(a)–(d) show the comparative evaluation of I_{ph}, $\mathscr{R}$, detectivity D, and external quantum efficiency EQE of the END$_1$–graphene hybrid and bare END$_1$ (insets) as a function of λ over T ranging from ~5.8 K to 298 K. The I_{ph} and $\mathscr{R}$ for END$_1$–graphene hybrids were found to be ~0.6 mA and just below $\sim 5 \times 10^9$ A W^{-1} at $\lambda \sim 400$ nm, while the bare END$_1$ devices (insets of Fig. 4(a) and (b)) show an $I_{ph} \sim 0.12$ mA and $\mathscr{R} \sim 2 \times 10^8$ A W^{-1}, respectively. A decrease in both parameters is seen for $\lambda \gtrsim 850$ nm over the temperatures tested. Moreover, D and EQE in Fig. 4(c) and (d) were calculated using $D\ (\text{Jones}) = \frac{\sqrt{A}}{\sqrt{2 \cdot e \cdot I_{dark}}}\mathscr{R}$, where $I_{dark} = 25.2$ mA, $A = 708.46$ μm^2 and $\text{EQE}\ (\%) = \frac{hc}{e \cdot \lambda}\mathscr{R}$, where $e = 1.6 \times 10^{-19}$ C is the electronic charge. The D and EQE of END$_1$–graphene hybrids were calculated to be $\sim 9.6 \times 10^{15}$ Jones and ~10^9 % at $T \sim 298$ K, respectively, as shown in Fig. 4(c) and (d), respectively. The D and EQE of the bare END$_1$ (insets of Fig. 4(c) and (d)) were measured to be ~10^{12} Jones and ~10^6 % at $T \sim 298$ K at $\lambda \sim 400$ nm. Again, both parameters decrease for $\lambda \gtrsim 850$ nm over the temperatures tested. It is notable that END$_1$ and END$_1$–graphene show an

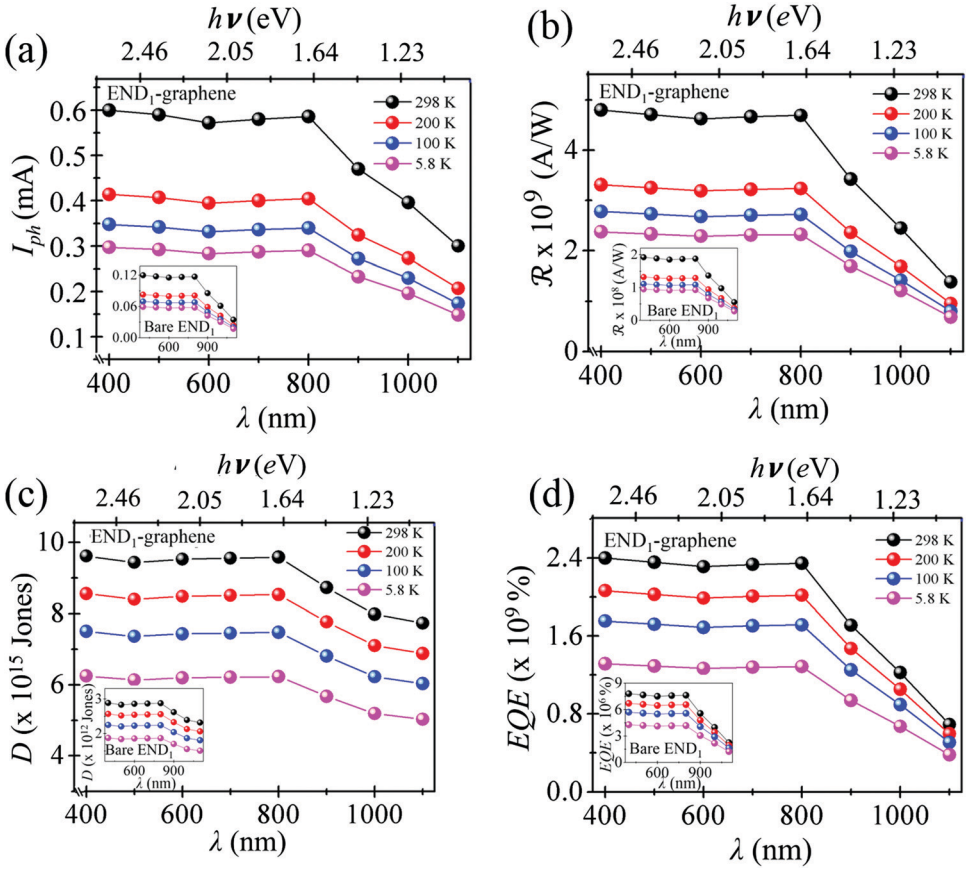

Fig. 4 (a)–(d) Comparative analysis of the T-dependent I_{ph}, $\mathscr{R}$, D, and EQE of END_1–graphene, and bare END_1 (insets) from $\lambda \sim 400$–1100 nm at various T. (a) For $\lambda \sim 400$ nm, the device shows high I_{ph} (~ 0.6 mA) and (b) high $\mathscr{R}$ (approaching 5×10^9 A W^{-1}) for END_1–graphene at $T \sim 298$ K and I_{ph} and $\mathscr{R}$ start to decrease for $\lambda \gtrsim 850$ nm. This decrease is due to the fact that an efficient photoconductance appears in the END_1 film at $h\nu \gtrsim 1.64$ eV (*i.e.* $\lambda \gtrsim 850$ nm). The (c) D and (d) EQE of END_1–graphene hybrids were calculated to be $\sim 9.6 \times 10^{15}$ Jones and $\sim 10^9$ % at ~ 298 K at $\lambda \sim 400$ nm, respectively. A similar trend was observed for the bare END_1 (insets of (a)-(d)) from $\lambda \sim 400$–800 nm. At $\lambda \sim 400$ nm, the I_{ph} and $\mathscr{R}$ for bare END_1 were ~ 0.12 mA and $\sim 2 \times 10^8$ A W^{-1}, and D and EQE for END_1 were $\sim 2.8 \times 10^{12}$ Jones and $\sim 10^6$ % at $T \sim 298$ K.

increase in photoresponse for $h\nu \gtrsim 1.64$ eV (*i.e.* $\lambda \leq 850$ nm), which demonstrates that the photoinduced carriers are only generated for λ below this value, where the carriers have sufficient energy to overcome the energy barrier. The values of I_{ph}, $\mathscr{R}$, D, and EQE are indeed enhanced significantly through the interaction of END_1 with graphene compared to the bare END_1 system. Additionally, the D and EQE are comparable to the previously reported values for graphene-perovskite ($MAPbI_3$) devices ($D \sim 10^{15}$ Jones and EQE $\sim 10^8$ %).[50]

2.2 Graphene–La@C_{82} hybrid

To delve further into the graphene–endohedral hybrid interaction, we conducted experiments with another endohedral fullerene, La@C_{82} denoted as END_2 here, that was deposited on top of the graphene. The same methodology was used to deposit END_2, as discussed in Section 2.1 for END_1. Before the preparation of the END_2–graphene hybrid devices, initial measurements were conducted on the bare END_2 as shown by the electrophoretic deposition data depicted for END_2 in Fig. S3, ESI† and to also measure the intrinsic conductance of these endohedrals. Further, AFM was used to determine the agglomeration of END_2 on top of the graphene membrane (Fig. S4, ESI†). The bare graphene thickness was ~ 12.8 nm measured using AFM indicating MLG. The cluster arrangement for END_2 on graphene is seen in Fig. S4(b)(i) and (ii) (ESI†).

The END_2–graphene hybrid was further characterized using Raman Spectroscopy, where Fig. 5(a) shows the Raman spectra of the END_2–graphene hybrid and the bare graphene at room T; the inset in Fig. 5(a) shows the Raman spectra of the bare END_2 film. The peaks at ~ 672 cm^{-1}, ~ 692 cm^{-1}, ~ 753 cm^{-1}, and ~ 792 cm^{-1} in the inset represent the intrinsic internal vibrational modes of END_2.[39] The G-peak of graphene experiences a $\Delta\omega^{(-)}$ shift of ~ 6 cm^{-1} (from ~ 1580 cm^{-1} to ~ 1574 cm^{-1}) as shown in the magnified plot of Fig. 5(b), while the 2D-peak undergoes a $\Delta\omega^{(-)}$ shift of ~ 12 cm^{-1} (from ~ 2704 cm^{-1} to ~ 2692 cm^{-1}) illustrated in Fig. 5(c). In the END_2–graphene hybrid, a peak at ~ 789 cm^{-1} (with relative normalized peak intensity for $I_{END_2} \sim 0.04$ a.u.) is seen, which for the bare END_2 film occurs at 792 cm^{-1}. This shift arises from the van der Waals interaction between END_2 and graphene. The La atom has three valence electrons in its outermost shell and has a strong tendency to donate electrons.[40] Also, from the Raman red shift of $\Delta\omega^{(-)}$ for the G- and the 2D-band, we infer that END_2 induces n-type doping in graphene, which is in alignment

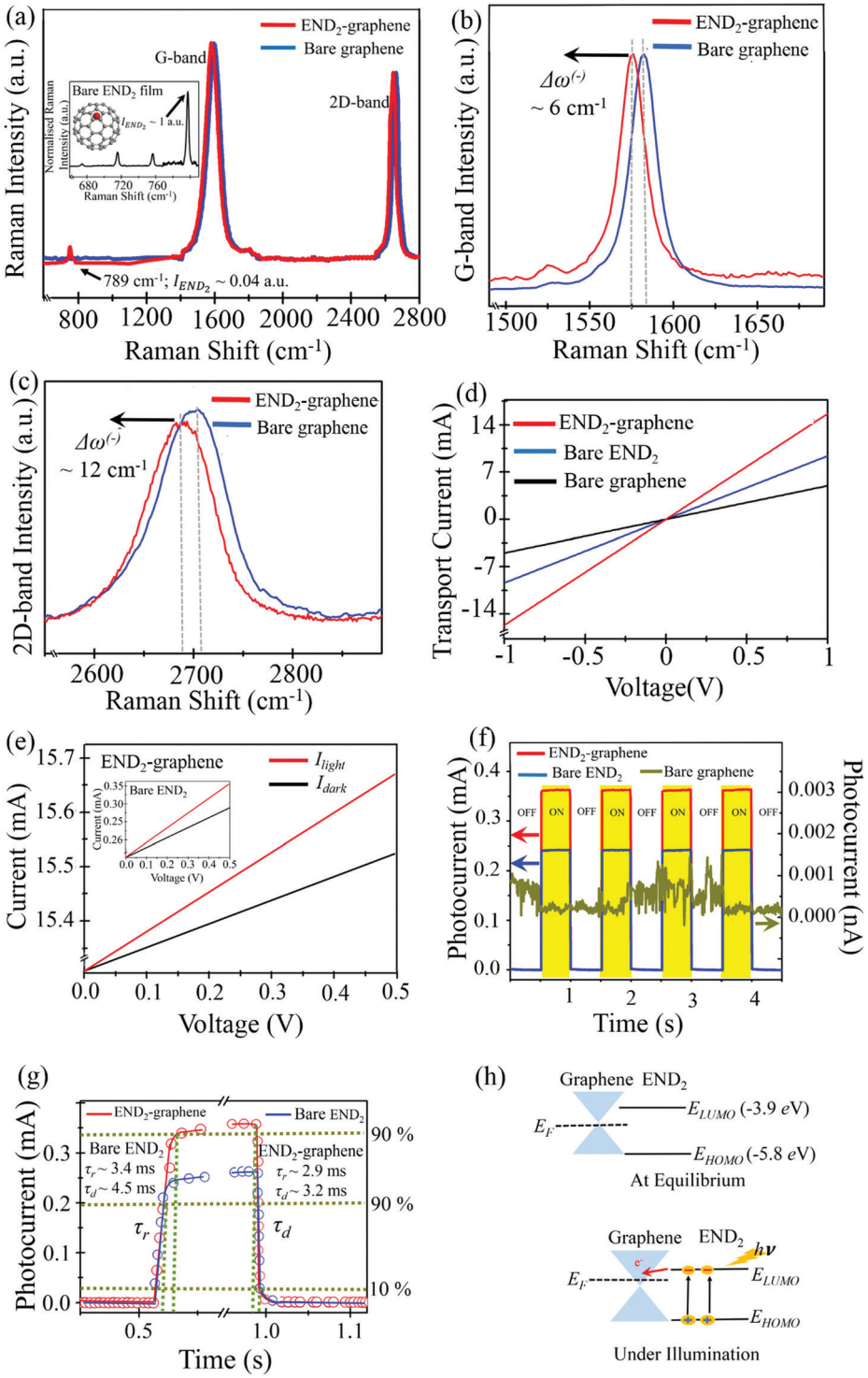

Fig. 5 (a) Raman spectra of END_2–graphene and bare graphene. Inset shows the Raman spectrum for the bare END_2 film. The peaks at ~672, 692, 753, and 792 cm^{-1} represent the internal vibrational modes of END_2. In the END_2–graphene hybrid, the main 792 cm^{-1} peak for END_2 shifts to ~789 cm^{-1} and is attributed to the van der Waals interaction between END_2 and graphene. (b) The G-band of graphene experiences a $\Delta\omega^{(-)}$ shift of ~6 cm^{-1} and (c) the 2D-band red-shifts by ~12 cm^{-1}. From the $\Delta\omega^{(-)}$ shift for the G- and the 2D-band it can be inferred that END_2 induces n-type doping in graphene. (d) The *I*–*V* Characteristics of the END_2–graphene hybrid, bare END_2, and bare graphene where transport is enhanced for the END_2–graphene hybrid device. (e) The *I*–*V* of the END_2–graphene hybrid and bare END_2 (inset) in the dark and illuminated states for a white light source at room *T*. (f) Pulsed ON (yellow) and OFF (no color) cycles showing the photoresponse for the three cases at 1 V bias (where, I_{light} ~ 16.15 mA and I_{dark} ~ 15.80 mA for END_2–graphene, and I_{light} ~ 0.61 mA and I_{dark} ~ 0.38 mA for END_2). (g) A magnified single ON-cycle pulse, where the τ_r and τ_d were calculated. Left and right insets show the values of τ_r and τ_d for bare END_2 and END_2–graphene hybrid, respectively. (h) Schematic representation of the energy band diagram for graphene and END_2 at equilibrium (top), and under illumination (bottom) illustrating the electron transfer from END_2 to graphene, inducing the n-type character in graphene.

with the oxidation potential for END_2 that is discussed in more detail below.

Electrical measurements of the END_2–graphene hybrid were compared to bare graphene and bare END_2 at room T, as shown in Fig. 5(d). The I_{dark} values were twice as high for the END_2–graphene hybrid relative to bare END_2. The hybrid also shows enhancement in optoelectronic transport properties when illuminated with a white light source as shown by the data in Fig. 5(e). The time-dependent I_{ph} of the END_2–graphene hybrid was also measured as shown in Fig. 5(f) for 1 V bias, and the results were compared with bare graphene and the bare END_2. The END_2–graphene hybrid exhibited the highest I_{ph}, while a negligible photoresponse resulted from the bare graphene device (secondary axis of Fig. 5(f)); here $I_{light} \sim 16.15$ mA and $I_{dark} \sim 15.80$ mA for END_2–graphene at 1 V, and $I_{light} \sim 0.61$ mA and $I_{dark} \sim 0.38$ mA for END_2 at $\sim$1 V. Also, τ_r and τ_d of END_2–graphene were measured in a similar fashion as for END_1, where $\tau_r \sim 2.9$ ms and $\tau_d \sim 3.2$ ms for the END_2–graphene hybrid, and $\tau_r \sim 3.4$ ms and $\tau_d \sim 4.5$ ms for bare END_2, as illustrated in Fig. 5(g). The $\mathscr{R}$ values of the END_2–graphene hybrid and bare END_2 were measured to be $\sim 2.8 \times 10^8$ A W^{-1} and $\sim 6 \times 10^7$ A W^{-1}, respectively, at room T. The band diagram was also postulated to explain the behaviour of the hybrid at equilibrium and under illumination, as shown schematically in Fig. 5(h) at equilibrium (top) and under illumination (bottom). Upon illumination, light is absorbed by END_2 and photo-generated carriers are created. Since a La atom has three valence electrons present in its shell and donates its electrons to the carbon cage, the LUMO level of END_2 is lowered to ~ -3.9 eV compared to END_1.[57] Thus, due to the electron-donating nature of La, n-type doping of graphene is observed.[58] Moreover, the oxidation potential of END_2 is found to be ~ 0.07 mV,[40] and given its low value, this again implies that END_2 is a relatively good electron-donor, which is also consistent with the Raman shift (red-shifted) observed in Fig. 5(b) and (c) for n-type doping in graphene. Doping effects can also be verified through back gating measurements on a future study. Since La@C_{82} induces n-doping in graphene, eqn (3) (applied for p-type doping in graphene)[55] is not applicable in order to calculate the magnitude of the E_F shift.

Similar to the measurements conducted using END_1, the END_2–graphene hybrid device was further exposed to a wide range of λ's from $\sim$400–1100 nm using a tunable laser source, as shown by the data for I_{ph}, $\mathscr{R}$, D, and EQE, in Fig. 6(a)–(d), respectively. The I_{ph}, in Fig. 6(a) was indeed higher for the END_2–graphene hybrid device compared to bare END_2, and an $\mathscr{R}$ of $\sim 10^8$ A W^{-1} was measured for the END_2–graphene hybrid compared to $\sim 10^7$ A W^{-1} for bare END_2, as shown in Fig. 6(b).

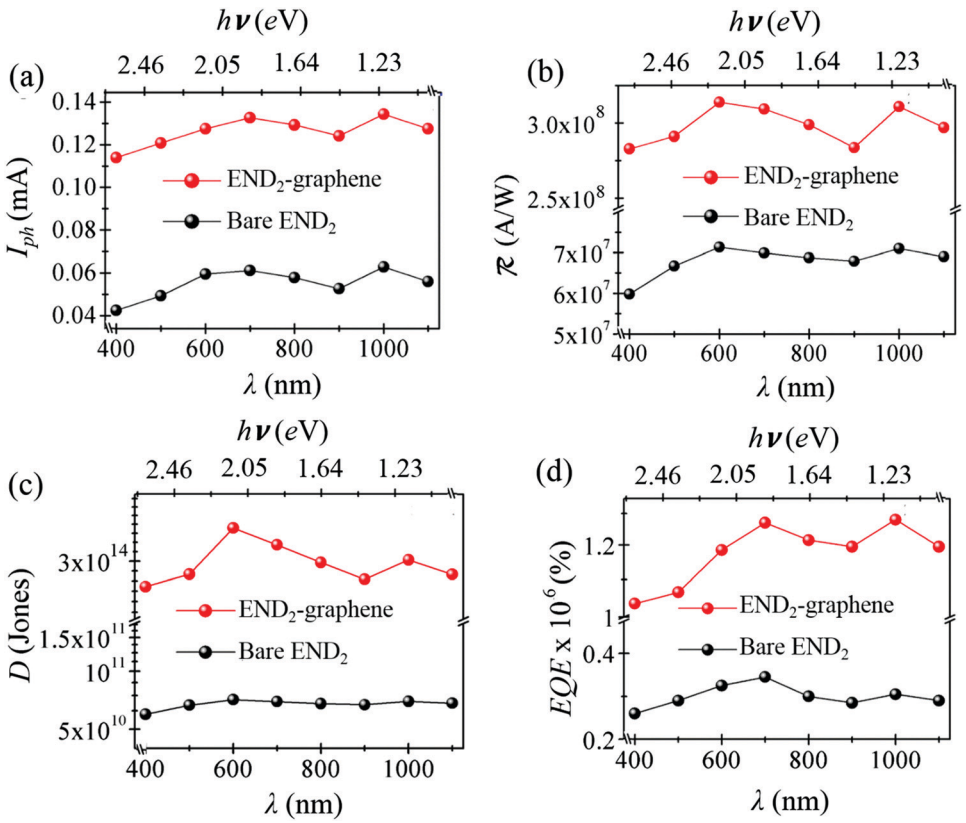

Fig. 6 The (a) I_{ph}, (b) $\mathscr{R}$, (c) D, and (d) EQE of the END_2–graphene hybrid and the bare END_2 from $\lambda \sim$ 400–1100 nm at room T. The devices were photo responsive with $\mathscr{R} \sim 10^8$ A W^{-1} for the END_2–graphene hybrid and $\sim 10^7$ A W^{-1} for END_2. The promising broadband optical absorption response with END_2 is attributed to the fact that END_2 shows broad absorption bands over the entire visible and near-IR regime. From the data in (c) and (d), the D and EQE of the hybrid device was found to be $\sim 10^{14}$ Jones and $\sim 10^6$ %, respectively.

Table 2 Our device results in comparison to prior reports for graphene hybrid structures. From the figures of merit, it is clear that the results reported here show the END_1 and END_2 graphene based hybrids enable exceptional performance improvements when compared to the prior literature. Here FLG refers to few-layer–graphene, and SLG refers to single-layer–graphene

Material	Detector type	λ (nm)	τ_r (ms)	τ_d (ms)	$\mathscr{R}$ (A W^{-1})	Power density (mW cm^{-2})	D (Jones), EQE (%)	Ref.
PbS QDs-SLG	Photo-gating	~400–700	~10	~20	~10^7	~0.2	D ~ 10^{13}	49
Bi_2Te_3-SLG heterostructure	Photo-gating	~980	~8.7	—	~35	—	—	51
Few layer MoS_2-SLG	Photo-gating	~635	—	—	~10^8	~6.4×10^4	—	8
C_{60}-SLG	Photo-gating	~200	—	—	~10^7	~5	EQE ~ 10^8	12
$FeCl_3$-FLG	Photo-conductive	~375	—	—	~10	~15.3	D ~ 10^3	25
Fluorographene (fluorinated MLG)	Photo-gating/photo-conductive	~255–4290	~80	~200	~10^3	~0.2	D ~ 10^{11}	24
Few layer MoS_2-glassy-graphene	Photo-conductive	~532	—	—	~0.012	—	D ~ 10^{10}	20
$MAPbI_3$-graphene	Photo-gating	~450–750	—	~879	~10^7	~15.4	D ~ 10^{15}, EQE ~ 10^8	50
END_1–MLG	**Photo-conductive**	**~400–1100**	**~1.8**	**~2.7**	**~10^9**	**~3**	***D* ~ 10^{15}, EQE ~ 10^9**	**This work**
END_2–MLG	**Photo-conductive**	**~400–1100**	**~2.9**	**~3.2**	**~10^8**	**~3**	***D* ~ 10^{14}, EQE ~ 10^8**	**This work**

What is distinctly clear from the data in Fig. 6 is the broad absorption occurring for the END_2–graphene hybrid over the entire ~400–1100 spectral range, which is in contrast to the data obtained for the END_1–graphene hybrid, where absorption decreased for $\lambda \gtrsim 850$ nm. This is due to the fact that END_2 shows broad absorption bands over the entire visible and near-IR regions, which was another unique reason for us to study the dynamics of this particular endohedral with graphene in a device platform.[59]

The D and EQE of the END_2–graphene hybrid device were calculated to be ~10^{14} Jones and ~10^6 %, respectively. We have compared our results with other graphene-based hybrid materials,[8,49–51] as shown in Fig. 6(c) and (d), and summarized in Table 2. It should be noted that the best $\mathscr{R} \sim 10^9$ A W^{-1} reported here for END_1–graphene fabricated in this study is ~10 times higher compared to previous MoS_2–graphene based photodetector[8] where an $\mathscr{R} \sim 10^8$ A W^{-1} was reported for $\lambda \sim$ 400–1100 nm. Our work clearly sets the stage for opening up avenues for a new class of endohedral-fullerene doped 2D–graphene hybrids to enable high performance optoelectronic devices in the future.

3. Conclusion

In summary, in this work photodetectors based on graphene–endohedral fullerenes were fabricated and characterized. From the Raman spectra analyses, confirmation of charge transfer processes occurring between the endohedral fullerenes and graphene is evident. The $\Delta\omega^{(+)}$ shift for the case of the END_1–graphene hybrid and $\Delta\omega^{(-)}$ shift in the END_2–graphene hybrid confirms that graphene acts as an electron donor in the former case, and as an electron acceptor in the latter case. Both END_1–graphene and END_2–graphene hybrid devices display a strong photoresponse under optical illumination. The photoinduced free holes (or electrons) are injected into graphene with END_1 (or END_2) which leads to high $\mathscr{R}$ and D for the hybrids. The $\mathscr{R}$, D, and EQE of the END_1–graphene hybrid reached values exceeding ~10^9 A W^{-1}, ~10^{15} Jones, and ~10^9 %, respectively. Similarly, the END_2–graphene hybrid exhibited values for $\mathscr{R}$, D, and EQE of ~10^8 A W^{-1}, ~10^{14} Jones, and ~10^6 %, respectively. Moreover, the optoelectronic response of the END_2–graphene hybrids showed a broadband response well into the IR up to 1100 nm, unlike the END_1–graphene hybrids where the photoresponse decreased for $\lambda \gtrsim 850$ nm. To the best of our knowledge, our results represent the first approach towards the fabrication of an endohedral fullerene–graphene-based photodetectors, which does not require a complicated fabrication process and yields the highest reported values for photodetector device figures of merit. The excellent performance of our endohedral-fullerene graphene hybrid photodetectors is exceptional and is bound to pave the way for a new class of hybrid 0D–2D graphene-based photonic devices in the future for imaging, surveillance and defense-related applications.

4. Methods

4.1 Materials

A 10 × 10 × 1 mm HOPG crystal from SPI Supplies Grade SPI-1 was mechanically exfoliated on top of a SiO_2/Si substrate using

residue-free blue tac tape from Semiconductor Corp resulting in a few layer graphene (FLG) membrane. The procedure for exfoliation adopted was similar to that described by Saenz *et al.*[60] A suspension of endohedral END_1 ($Sc_3N@C_{80}$) (LUNA LnW-0920, END_1 Trinetasphere, $\gtrsim$95%) at different concentrations in $\sim$1 mL of *o*-DCB was electrophoretically deposited on the graphene membrane. Endohedral END_2 ($La@C_{82}$) was prepared using a Krätschmer–Huffman arc discharge generator and purified using HPLC after extracting the soot with toluene as previously described.[28,59]

4.2 Characterization

Optical absorption spectroscopy was conducted using a CARY 5000 spectrophotometer in quartz cuvettes with $\sim$0.3 mL volumetric capacity. The SEM imaging was carried out with a Hitachi S-4800. For AFM, the images were acquired using a Veeco Microscope at ambient air conditions (relative humidity $\sim$30%) with $k \sim 0.3$ N m^{-1} for the silicon tip (provided by Ted Pella Inc.) in contact mode. The Raman data was gathered using a Horiba LabRAM HR Evolution, where the excitation λ used was $\sim$532 nm.

4.3 Device fabrication and measurements

The devices were fabricated using a photolithography process for metal contact patterning on a $\sim$270 nm SiO_2/Si substrate. The electrodes were patterned on a graphene membrane using a Karl Suss MJB3 mask aligner.[60] Then, $\sim$10 nm of Ti and $\sim$100 nm of Au were deposited using an e-beam evaporator, followed by metal lift-off. The electronic and optoelectronic device characterization was conducted using a Lakeshore CRX-4K cryogenic probe stage with T control from $\sim$5.8 K to 298 K and a low noise semiconductor parameter analyzer, the Keysight B1500A was used for the low-noise electronic transport measurements. The photoresponse was measured at room T by illuminating the device with a broadband light source (LEDR/4 type illuminator) which has a color T of $\sim$6500 K. The tunable spectral measurements from $T \sim$ 5.8 K to $\sim$298 K were conducted using a tunable laser source, the Fianium LLFT Contrast from NKT Photonics. Both the broadband and narrow-band sources were calibrated using the Thorlabs optical power meter PM100D.

Conflicts of interest

There are no conflicts to declare.

Acknowledgements

We would like to thank Ben Sarota and Sangram Mazumder at UNT who assisted with the Au/Ti deposition. We greatly appreciate the support received from the Air Force Office of Scientific Research (grant number FA9550-15-1-0200), the Army Research Office (grant number W911NF-15-1-0425) and the National Science Foundation (grant number NSF ECCS 1753933) that enabled us to pursue this work. A. B. K. is also grateful to the support received from the UNT Start-up package and the PACCAR Technology Institute and Endowed Professorship. L. E. thanks the NSF for generous support of this work under grant (CHE-1801317) and to the NSF-PREM program (DMR-1205302). The Robert A. Welch Foundation is also gratefully acknowledged for an Endowed Chair to L. E. (grant AH-0033).

References

1 F. Bonaccorso, Z. Sun, T. Hasan and A. C. Ferrari, *Nat. Photonics*, 2010, **4**, 611.
2 K. S. Novoselov, D. Jiang, F. Schedin, T. J. Booth, V. V. Khotkevich, S. V. Morozov and A. K. Geim, *Proc. Natl. Acad. Sci. U. S. A.*, 2005, **102**, 10451.
3 A. C. Ferrari, F. Bonaccorso, V. Fal'ko, K. S. Novoselov, S. Roche, P. Bøggild, S. Borini, F. H. L. Koppens, V. Palermo, N. Pugno, J. A. Garrido, R. Sordan, A. Bianco, L. Ballerini and J. Kinaret, *Nanoscale*, 2015, **7**, 4598.
4 Z. Sun, T. Hasan, F. Torrisi, D. Popa, G. Privitera, F. Wang, F. Bonaccorso, D. M. Basko and A. C. Ferrari, *ACS Nano*, 2010, **4**, 803.
5 A. B. Kaul, *J. Mater. Res.*, 2014, **29**, 348.
6 H. Zhou, T. Gu, J. F. McMillan, M. Yu, G. Lo, D. L. Kwong, G. Feng, S. Zhou and C. W. Wong, *Appl. Phys. Lett.*, 2016, **108**, 1.
7 F. Xia, T. Mueller, Y. Lin, J. Tsang and M. Freitag, *Nano Lett.*, 2009, **9**, 1039.
8 K. Roy, M. Padmanabhan, S. Goswami, T. P. Sai, G. Ramalingam, S. Raghavan and A. Ghosh, *Nat. Nanotechnol.*, 2013, **8**, 826.
9 D. Fadil, R. F. Hossain, G. A. Saenz and A. B. Kaul, *J. Mater. Chem. C*, 2017, **5**, 5323.
10 G. Jnawali, Y. Rao, J. H. Beck, N. Petrone, I. Kymissis, J. Hone and T. F. Heinz, *ACS Nano*, 2015, **9**, 7175.
11 C. O. Aristizabal, E. J. G. Santos, S. Onishi, A. Yan, H. I. Rasool, Y. Lv, D. Latzke, J. V. Jr, M. F. Crommie, M. Sorensen, C. Lin, K. Watanabe, T. Taniguchi, A. Lanzara and A. Zettl, *ACS Nano*, 2017, **11**, 4686.
12 S. Qin, X. Chen, Q. Du, Z. Nie, X. Wang, H. Lu, X. Wang, K. Liu, Y. Xu, Y. Shi, R. Zhang and F. Wang, *ACS Appl. Mater. Interfaces*, 2018, **10**, 38326.
13 J. Correa, P. Orellana and M. Pacheco, *Nanomaterials*, 2017, **7**, 69.
14 E. J. G. Santos, D. Scullion, X. S. Chu, D. O. Li, N. P. Guisinger and Q. H. Wang, *Nanoscale*, 2017, **9**, 13245.
15 J. A. Rather, E. A. Khudaish, A. Munam, A. Qurashi and P. Kannan, *Sens. Actuators, B*, 2016, **237**, 672.
16 D. Yu, K. Park, M. Durstock and L. Dai, *J. Phys. Chem. Lett.*, 2011, **2**, 1113.
17 K. Kim, T. H. Lee, E. J. G. Santos, P. S. Jo, A. Salleo, Y. Nishi and Z. Bao, *ACS Nano*, 2015, **9**, 5922.
18 B. Kang, Y. Kim, W. J. Yoo and C. Lee, *Small*, 2018, **14**, 1802593.
19 R. F. Hossain, I. G. Deaguero, T. Boland and A. B. Kaul, *npj 2D Mater. Appl.*, 2017, **1**, 28.
20 H. Xu, X. Han, X. Dai, W. Liu, J. Wu, J. Zhu, D. Kim, G. Zou, K. A. Sablon, A. Sergeev, Z. Guo and H. Liu, *Adv. Mater.*, 2018, **30**, 1706561.

21 L. H. Li, T. Tian, Q. Ca1, C. J. Shih and E. J. G. Santos, *Nat. Commun.*, 2018, **9**, 1271.
22 T. H. Lee, K. Kim, G. Kim, H. J. Park, D. Scullion, L. Shaw, M. Kim, X. Gu, W. Bae, E. J. G. Santos, Z. Lee, H. S. Shin, Y. Nishi and Z. Bao, *Chem. Mater.*, 2017, **29**, 2341.
23 A. Pinkard, A. M. Champsaur and X. Roy, *Acc. Chem. Res.*, 2018, **51**, 919.
24 S. Du, W. Lu, A. Ali, P. Zhao, K. Shehzad, W. Yin, J. Luo, B. Yu, T. Hasan, Y. Xu, W. Hu and X. Duan, *Adv. Mater.*, 2017, **29**, 1700463.
25 A. De Sanctis, G. F. Jones, D. J. Wehenkel, F. Bezares, F. H. L. Koppens, M. F. Craciun and S. Russo, *Sci. Adv.*, 2017, **3**, 1602617.
26 N. F. Montcada, S. Arrechea, A. Molina-Ontoria, A. I. Aljarilla, P. de la Cruz, L. Echegoyen, E. Palomares and F. Langa, *Org. Electron.*, 2016, **38**, 330.
27 M. Vizuete, M. Barrejón, M. J. Gómez-Escalonilla and F. Langa, *Nanoscale*, 2012, **4**, 4370.
28 A. A. Popov, S. Yang and L. Dunsch, *Chem. Rev.*, 2013, **113**, 5989.
29 M. N. Chaur, F. Melin, A. L. Ortiz and L. Echegoyen, *Angew. Chem., Int. Ed.*, 2009, **48**, 7514.
30 J. U. Reveles, N. N. Karle, T. Baruah and R. R. Zope, *J. Phys. Chem. C*, 2016, **120**, 26083.
31 J. R. Pinzón, D. C. Gasca, S. G. Sankaranarayanan, G. Bottari, T. Torres, D. M. Guldi and L. Echegoyen, *J. Am. Chem. Soc.*, 2009, **131**, 7727.
32 I. Jeon, H. Ueno, S. Seo, K. Aitola, R. Nishikubo and A. Saeki, *Angew. Chem.*, 2018, **130**, 4697.
33 R. B. Ross, C. M. Cardona, D. M. Guldi, S. G. Sankaranarayanan, M. O. Reese, N. Kopidakis, J. Peet, B. Walker, G. C. Bazan, E. Van Keuren, B. C. Holloway and M. Drees, *Nat. Mater.*, 2009, **8**, 208.
34 M. Liedtke, A. Sperlich, H. Kraus, A. Baumann, C. Deibel, M. J. M. Wirix, J. Loos, C. M. Cardona and V. Dyakonov, *J. Am. Chem. Soc.*, 2011, **133**, 9088.
35 Y. Xu, J. Guo, T. Wei, X. Chen, Q. Yang and S. Yang, *Nanoscale*, 2013, **5**, 1993.
36 S. Nagase and K. Kdmyashi, *Chem. Phys. Lett.*, 1994, **231**, 319.
37 K. Harigaya and S. Abe, *Phys. Rev. B: Condens. Matter Mater. Phys.*, 1994, **49**, 16746.
38 S. Stevenson, G. Rice, T. Glass, K. Harlch, F. Cromer, M. R. Jordan, J. Craft, E. Hadju, R. Bible, M. M. Olmstead, K. Maltra, A. J. Fisher, A. L. Balch and H. C. Dorn, *Nature*, 1999, **401**, 55.
39 S. Lebedkin, B. Renker, R. Heid, H. Schober and H. Rietschel, *Appl. Phys. A: Mater. Sci. Process.*, 1998, **66**, 273.
40 Y. Takano, *Fullerenes, Nanotubes, Carbon Nanostruct.*, 2014, **22**, 243.
41 M. Rudolf, S. Wolfrum, D. M. Guldi, L. Feng, T. Tsuchiya, T. Akasaka and L. Echegoyen, *Chem. – Eur. J*, 2012, **18**, 5136.
42 A. C. Ferrari, J. C. Meyer, V. Scardaci, C. Casiraghi, M. Lazzeri, F. Mauri, S. Piscanec, D. Jiang, K. S. Novoselov, S. Roth and A. K. Geim, *Phys. Rev. Lett.*, 2006, **97**, 1.
43 S. Tian, Y. Yang, Z. Liu, C. Wang, R. Pan, C. Gu and J. Li, *Carbon*, 2016, **104**, 27.
44 I. Calizo, A. A. Balandin, W. Bao, F. Miao and C. N. Lau, *Nano Lett.*, 2007, **7**, 2645.
45 B. Davaji, H. D. Cho, M. Malakoutian, J. K. Lee, G. Panin, T. W. Kang and C. H. Lee, *Sci. Rep.*, 2017, **7**, 1.
46 J. Schiefele, F. Sols and F. Guinea, *Phys. Rev. B: Condens. Matter Mater. Phys.*, 2012, **85**, 195420.
47 Y. Liu, Z. Liu, W. Lew and Q. Wang, *Nanoscale Res. Lett.*, 2013, **8**, 335.
48 M. Michel, C. Biswas, C. S. Tiwary, G. A. Saenz, R. F. Hossain, P. Ajayan and A. B. Kaul, *2D Mater.*, 2017, **4**, 025076.
49 D. Zhang, L. Gan, Y. Cao, Q. Wang, L. Qi and X. Guo, *Adv. Mater.*, 2012, **24**, 2715.
50 P. H. Chang, S. Y. Liu, Y. B. Lan, Y. C. Tsai, X. Q. You, C. S. Li, K. Y. Huang, A. S. Chou, T. C. Cheng, J. K. Wang and C. I. Wu, *Sci. Rep.*, 2017, **7**, 1.
51 H. Qiao, J. Yuan, Z. Xu, C. X. Pan, S. Li and Q. Bao, *ACS Nano*, 2015, **9**, 1886.
52 A. Sharma, R. Kumar, B. Bhattacharyya and S. Husale, *Sci. Rep.*, 2016, **6**, 1.
53 J. P. Phillips, B. Koene and S. R. Wilson, *Luna innovations, US Pat.*, 20080085234, 2008.
54 A. Das, S. Pisana, S. Piscanec, B. Chakraborty, S. K. Saha, U. V. Waghmare, R. Yiang, H. R. Krishnamurhthy, A. K. Geim, A. C. Ferrari and A. K. Sood, *Nat. Nanotechnol.*, 2007, **3**, 1.
55 C. Bautista-Flores, R. Y. Sato-Berrú and D. Mendoza, *J. Mater. Sci. Chem. Eng.*, 2015, **3**, 17.
56 C. Casiraghi, S. Pisana, K. S. Novoselov, A. K. Geim and A. C. Ferrari, *Appl. Phys. Lett.*, 2007, **91**, 12.
57 K. Shibata, Y. Rikiishi, T. Hosokawa, Y. Haruyama, Y. Kubozono, S. Kashino, T. Uruga, A. Fujiwara, H. Kitagawa, T. Takano and Y. Iwasa, *Surf. Sci.*, 2003, **522**, 1.
58 S. Pang, H. N. Tsao, X. Feng and K. Mullen, *Adv. Mater.*, 2009, **21**, 3488.
59 T. Akasaka, T. Wakahara, M. Kako, Y. Nakadaira and R. Nagahata, *J. Am. Chem. Soc.*, 2000, **122**, 9316.
60 G. A. Saenz, G. Karapetrov, J. Curtis and A. B. Kaul, *Sci. Rep.*, 2018, **8**, 1.